1   **Large enhancements in southern hemisphere satellite-observed trace gases due to the 2019/2020**

2   **Australian wildfires**

3   Richard J. Pope[1,2], Brian J. Kerridge[3,4], Richard Siddans[3,4], Barry G. Latter[3,4], Martyn P. Chipperfield[1,2],

4   Stephen R. Arnold[1], Lucy J. Ventress[3,4], Matilda A. Pimlott[1], Ailish M. Graham[1], Diane S. Knappett[3,4]

5   and Richard Rigby[1,5]

6

7   *1: School of Earth and Environment, University of Leeds, Leeds, United Kingdom*

8   *2: National Centre for Earth Observation, University of Leeds, Leeds, United Kingdom*

9   *3: Remote Sensing Group, STFC Rutherford Appleton Laboratory, Chilton, United Kingdom*

10   *4: National Centre for Earth Observation, STFC Rutherford Appleton Laboratory, Chilton, United*

11   *Kingdom*

12   *5: Centre for Environmental Modelling and Computation, University of Leeds, Leeds, United Kingdom*

13

14   Submitted to *Journal of Geophysical Research: Atmospheres*

15

16   **Key Points**

17   • Satellite-retrieved carbon monoxide (CO) plumes from the Australian fires circumvent the
18   Southern Hemisphere.

19   • Satellite-retrieved methanol (CH_3OH) shows downwind enhancement of CH_3OH:CO ratio
20   suggesting in-plume secondary CH_3OH production as well as direct emission.

21

22   **Key Words**

23   Australian Fires; IASI; Carbon Monoxide; Methanol; Methane

24   **Abstract:**

25   The 2019/2020 Australian wildfires emitted large quantities of atmospheric pollutant gases and
26   aerosols. Using state-of-the-art near-real-time satellite measurements of tropospheric composition,
27   we present an analysis of several emitted trace gases and their long-range transport, and compare
28   to the previous (2018/2019) fire season. Observations of carbon monoxide (CO) show that fire
29   emissions were so intense that the distinct Australian fire plume managed to circumnavigate the
30   Southern Hemisphere (SH) within a few weeks, with eastward propagation over the South Pacific,

South America, the South Atlantic, Africa and the Indian Ocean. Elevated atmospheric methane levels were also detected in January 2020 fire plumes over the Pacific, defined using CO as a plume tracer, even though sampling was restricted spatially by aerosols and clouds. Observations also show significant enhancements of methanol from the fires, where $CH_3OH:CO$ enhancement ratios increased within the aged plume downwind over the South Pacific indicating secondary in-plume CH_3OH formation.

1. Introduction

Vegetation fires occur regularly in Australia between the months of August and December (Giglio et al., 2013; van der Werf et al., 2017). Burning activity predominantly occurs in northern Australia, but is widespread across the continent (Andela et al., 2017). Giglio et al., (2013) suggested that the majority of vegetation fires take place on savanna and shrubland, but in south-eastern Australia forest fires are most prevalent (Bradstock et al., 2012; van der Werf et al., 2010). Over recent decades, there have been large-scale decreases in Australian fire activity (Andela et al., 2017; Rabin et al., 2015). However, with present and future climate and land-use change, conditions in Australia are predicted to yield more frequent large-scale fire events (Pitman et al., 2007; Clarke et al., 2011; Di Virgilio et al., 2019). According to the Australian Bureau of Meteorology (2020), the 2019 summer was the warmest (1.52°C above the national average, 1961-1990) and driest (rainfall 40% lower than average) season on record. This provided suitable conditions for wildfires to ignite and spread.

The Australian wildfires of the 2019/2020 fire season, colloquially known as the "black summer", represented some of the largest events in recent decades. The fires burned over 110,000 km^2 of bush, forest and parks (BBC, 2020). The majority of the fire activity occurred in south-eastern Australia (New South Wales and Victoria), which is predominantly eucalyptus forest and woodland (SOTE, 2016). The fires caused 33 deaths (BBC, 2020) and killed over approximately 1 billion animals (UoS, 2020). In comparison, the Black Saturday fires (February 2009) in Victoria burned approximately 4500 km^2 and killed 173 people (Siddaway and Petelina, 2011). Though the 2019/2020 fire death toll was lower, the burned area was much larger producing substantial quantities of smoke and pollutants.

Vegetation fires emit large quantities of smoke/aerosols and trace gases, which have important impacts on climate and the atmospheric radiation balance (Li et al., 2017, Rowlinson et al., 2019) and surface air quality (AQ, Bowman and Johnston, 2005; Haikerwal et al., 2016; Reisen et al., 2005; Kiely et al., 2019). The 2019/2020 Australian fires emitted approximately 250 million tonnes of carbon dioxide (CO_2), equivalent to nearly half the country's annual anthropogenic emissions (Hope, 2020).This combination of fuel type, fire intensity and coverage, yielded large-scale fire plumes causing intense local pollution as well as long-range pollution transport. Wildfire-driven pyro-convection propagated vertically up into the stratosphere, reaching approximately 30 km (Ohneiser et al., 2020) over the South Pacific. In comparison, the Black Saturday fire plume reached 22 km (Siddaway and Petelina, 2011).

In this study, we use state-of-the-art satellite retrievals to provide detailed analysis of the spatial and temporal evolution of several trace gas distributions sourced from the 2019/2020 Australian fires. While available for the stratosphere, such capabilities were in their infancy when previous major burning events occurred in Australia (e.g. February 2009).

2. Observations
2.1 Fire Data Sets

We use two different satellite-derived fire activity datasets: fire radiative power (FRP) from the Global Fire Assimilation System (GFAS vn1.2; Kaiser et al., 2012) and burned area (BA) from the Fire INventory from NCAR (FINN near-real-time (NRT) vn1.0; Wiedinmyer et al., 2011). Both products are provided at a daily temporal resolution and are based on direct Moderate Resolution Imaging Spectroradiometer (MODIS) measurements (e.g. FRP and thermal anomalies). These quantities are merged with secondary information (including land surface type and emission factors) to derive top-down emissions for trace gases and aerosols (Kiely et al., 2019; Wooster et al., 2018).

2.2 Trace Gas Data Sets

In this study we use trace gas retrievals from the Infrared Atmospheric Sounding Interferometer (IASI). IASI is a Michelson interferometer which observes the spectral range 645 to 2760 cm^{-1} with spectral sampling of 0.25 cm^{-1} (Illingworth et al., 2011). It measures simultaneously in four fields of view (FOV, each circular at nadir with a diameter of 12 km) which are scanned across track to sample a 2200 km-wide swath (Clerbaux et al., 2009). IASI is one of a suite of nadir-sounders flying on Eumetsat's MetOp-A, -B and -C satellites in sun-synchronous polar orbits with equator crossing times of 9.30 (day) and 21.30 (night). Here we use CO, methanol (CH_3OH) and methane (CH_4) data from MetOp-B produced by NRT processing systems developed by the Rutherford Appleton Laboratory (RAL). CO profiles are co-retrieved with column amounts of CH_3OH, other trace gases and dust in an extended version of RAL's Infrared-Microwave-Sounding (IMS) scheme, which is described in the supplementary material (**SM-2**). IMS was developed originally to retrieve temperature, water vapour, ozone, surface spectral emissivity and cloud jointly from co-located measurements by IASI, the Microwave Humidity Sounder (MHS) and the Advanced Microwave Sounding Unit (AMSU-A) on MetOp. CH_4 data are retrieved by an improved version of the IASI scheme reported by RAL Space (2015), which is detailed by Siddans et al. (2017). Data are available from the Centre of Environmental Data Analysis (CEDA, Siddans et al., 2020). CO and CH_3OH have been quality filtered for a geometric cloud fraction of 0.5 or less (0.1 or less for CH_4 given the greater sensitivity to interference from cloud/aerosol) and a cost value of 1000.0 or less (120 or less for CH_4 plus a convergence flag equally 1.0). For CO and CH_3OH, we experimented with a stricter geometric cloud fraction threshold of <0.2. We found this had negligible impact on the scientific results, but did reduce the spatial coverage, making the fire signals noisier. Hence we used the <0.5 cloud fraction threshold. We have also investigated more localised enhancements in tropospheric column nitrogen dioxide ($TCNO_2$) from the Tropospheric Monitoring Instrument (TROPOMI) on-board ESA's Sentinel 5 – Precursor (S5P) satellite, which is discussed in the SM (see **SM-1**).

3. Results
3.1 Fire Activity

During the 2019/2020 fire season (November-December-January, NDJ), satellite observations detected substantially larger fire activity on the Australian south-eastern coastline around highly populated regions such as Sydney compared to the average of the previous 10 seasons (NDJ 2009-2019 climatology). GFAS FRP suggests that on average (NDJ climatology) (**Figure 1a**) there was limited fire activity over south-eastern Australia (i.e. 10-20 mW/m^2). The peak activity was more widespread across the north-western territories with FRP typically between 20 and 30 mW/m^2. However, in NDJ 2019/2020 the entire Australian south-eastern coastline experienced large-scale fires with intensities well above 50 mW/m^2 (**Figure 1b**). This is supported by the FINN BA (**Figure 1c & d**) with fire events peaking above 10 km^2 widespread across the south-east coast. In contrast, the

fire events in the NDJ climatology predominantly occurred over the north-western territories and northern coastlines, with lower BA between 3.0 and 7.0 km^2. **Figure 1e** shows the time-series of the total daily Australian FRP and BA for the climatological (median daily totals, 2009-2019) and 2019/2020 fire seasons. Between 1st November and 31st January, the climatological FRP has a small range (i.e. 25th-75th percentiles) between approximately 0 and 10 GW. Climatological BA ranges between approximately near-zero and 1700 km^2. However, the 2019/2020 FRP (BA) is typically between 20 (100) and 150 (1700) GW (km^2), but with peaks in late December (FRP=~320 GW, BA=~2200 km^2) and early January (FRP=~580 GW, BA=~3000 km^2). The peak FRP and BA values sit well outside the variability of the climatologies, highlighting the extreme fire activity experienced in the 2019/2020 fire season.

3.2 Carbon Monoxide

The 2019/2020 Australian fire season produced extensive quantities of emitted CO, as observed by IASI. **Figure 2c** shows a large total-column CO (TCCO) plume originating over south-eastern Australia and propagating across the entire Pacific, reaching South America. Here, the TCCO ranges between approximately 16-21 ×10^{17} molecules/cm^2, peaking over the Australian coastline and midway between continents in the NDJ period 2019/2020. In the previous burning season (NDJ 2018/2019), TCCO was considerably lower and ranged between 10-13 ×10^{17} molecules/cm^2, with no obvious fire signal over Australia (**Figure 2a**). **Figure 2e** shows the difference between fire seasons to be widespread and large (1.5-7.5 ×10^{17} molecules/cm^2) across the Pacific. Peak inter-year differences of over 5.0 ×10^{17} molecules/cm^2 occur over south-eastern Australia and the mid-Pacific, as the plume propagates eastwards. The inter-year differences are significant over large areas (99% confidence level based on the student t-test and where absolute mean differences are greater than 1.0 ×10^{17} molecules/cm^2) as shown by the green polygon-outlined regions.

During the 2018/2019 season, fire plumes of limited extent were detected, with moderate CO outflow from the east coast in November 2018 peaking at approximately 19.0 ×10^{17} molecules/cm^2 (**Figures 2b & d**). In NDJ 2019/2020, there is large and frequent CO outflow throughout the entire season. TCCO peaks at more than 30.0 ×10^{17} molecules/cm^2 and persists across the 20°-40°S band. **Figure 2f** shows that the inter-year difference exceeds 15.0 ×10^{17} molecules/cm^2 and the larger quantities of CO propagating out into the Pacific (**Figure 2c**). CO outflow from the peak fire activity (**Figure 1e**) in late December 2019/early January 2020 went on to circumnavigate the entire SH (**Figure 3**). Between 27th December 2019 and 9th January 2020, the fire emissions led to large quantities of CO (>25 ×10^{17} molecules/cm^2), which formed large-scale plumes propagating towards South America. Pyroconvection during this period uplifted plumes to altitudes where CO and other trace gases could more easily be detected by IASI (i.e. colder temperatures and above clouds). In the following fortnight, 10th – 23rd January 2020, these plumes reached South America (peak TCCO >20.0×10^{17} molecules/cm^2) and started propagating into the South Atlantic (15-18×10^{17} molecules/cm^2). A week later, the TCCO plume reached southern Africa (no local fire sources apparent there, unlike e.g. 15th-28th November 2019) with values still between 15-18×10^{17} molecules/cm^2. The TCCO quantities were also enhanced to 14-16×10^{17} molecules/cm^2 over the Indian Ocean, reaching the Australian west coastline and fully encircling the SH. Over south-eastern Australia (black box in **Figure S1c**), the 2019/2020 fires (NDJ) emitted 9.06 Tg of CO (1.73 times larger than the 2018/2019 annual total anthropogenic Australian CO emissions; NPI, 2020) in comparison to 0.33 Tg in NDJ 2018/2019, based on FINN emissions.

3.3. Methanol and Methane

Focusing on the 3rd – 16th of January 2020, when the fire plumes were most spatially extensive (see TCCO in **Figure 3**, **Figure 4a**), CH_3OH and CH_4 both showed substantial increases from the fires (**Figures 4b & c**). Total column CH_3OH (TCCH$_3$OH), relative to the 3rd – 16th January 2019, show peak enhancements of over 10×10^{15} molecules/cm^2 co-locating with TCCO enhancements of over 15×10^{17} molecules/cm^2 (**Figure 4a**). Though CH_3OH infrared absorption features are much weaker than those of CO and low background CH_3OH abundances (e.g. over the ocean) are difficult to detect in individual soundings (i.e. large estimated errors; see **SM-3**, **Figure S6**), robust signals are detected in large sources such as the Australian fire plume (i.e. >15×10^{15} molecules/cm^2, **Figure 5b, SM-3, Figure S7**).

CH_4, on spatial and temporal scales observable by satellite fluctuates by only a few % of its global mean value, unlike the order of magnitude of variability in CO and methanol. To retrieve CH_4 perturbations at the % level requires careful handling of cloud and, in the case of the Australian wildfire plumes, also smoke (and dust). As shown in **SM-4** and **Figure SM8**, IASI detects daily CO plumes, but the corresponding CH_4 distribution is less well sampled due to stringent filtering necessary for cloud. However, the column average CH_4 (CACH$_4$) anomaly for the 3rd-16^{th}January 2020, with reference to the de-trended and de-seasonalised multi-annual mean for January (2007-17, MetOp-A & B offline version) (**Figure 4c**) is positive over much of the region (e.g. ~0.01 ppmv), and some features (e.g. 0.015-0.03 ppmv) cohere with prominent structure (e.g. over the central South Pacific) in the CO and CH_3OH plumes (see **Figure 4a & b**). Therefore, we use CO as an in-plume tracer to quantify the much lower amplitude CH_4 signals from the fires. **Figure 4d** shows the time evolution of in-plume column average CO (CACO) and CACH$_4$ averaged over 150°E-90°W, 50-20°S (black box in **Figure S8**). The in-plume thresholds for CACO and CACH$_4$were set at 0.07 ppmv and 1.75 ppmv. Both thresholds had to be met, along with stringent cloud screening and other quality control for CH_4, in order for the pair of CO and CH_4 soundings at a given location to be sampled.

In the first two weeks of January 2020, the in-plume domain-averaged daily CACO ranges between 0.09 and 0.12 ppmv, and the standard deviation indicates large spatial variability. In the second two weeks of January, the spatially-averaged CACO is substantially lower, ranging between 0.07 and 0.08 ppmv, with much smaller spatial variability, consistent with mixing with neighbouring CO-poor airmasses in the east and less intense incoming plumes in the west. In contrast, for CACH$_4$ the spatially averaged value drops only slightly and spatial variability is unchanged in the second two weeks, attributable to mixing with high CH_4 tropical airmasses in the east. The peak average CACH$_4$values (1.78-1.79 ppmv) occur in the first few weeks and then 27th-29th January. Temporal correlation of the spatially averaged CO and CH_4 time series is 0.63 for the whole month and 0.86 between 1st and 20^{th}January. The daily spatial correlation in this period is between 0.2 and 0.5, indicative of a substantial fire-induced component of CH_4. In the latter period of January (21st-31st) the correlation drops below 0.0 indicating the fire-induced component to be less significant for CH_4 in comparison to other processes. Overall, the relationship between CO and CH_4 in data produced from IASI on MetOp-B demonstrates that the plumes emitted from the Australian fires contained CH_4 as well as CO. Emission factors of CH_4 from vegetation fires have been shown to be similar in magnitude to those of methanol on a mass emitted per mass of dry matter consumed basis (Agaki et al., 2011). It is worth noting that given the long CH_4 lifetime against hydroxyl radical (OH) oxidation (~9 years (McNorton et al., 2016)), any enhancement in methane due to OH suppression in the plume on the transport timescale of a few days would be minimal (~0.1% over 3 days under complete suppression of OH oxidation).

210

3.4. Enhancement Ratios

We investigate how the TCCH$_3$OH:TCCO enhancement ratio changes as the fire plume traverses the Pacific across the four regional boxes defined in **Figure 5a** between the 1st and 17th January 2020 (i.e. period of large fire plume). Box 1 covers the primary fire region and Boxes 2-4 cover the downwind outflow. In all cases, we see TCCO-TCCH$_3$OH correlation values (R in **Figure 5c-f**) above 0.63, peaking at 0.92 in Box 3, indicative of common origins. The in-plume TCCO and TCCH$_3$OH values are defined based on a subjectively chosen threshold (TCCO = 18.0×10^{17} molecules/cm^2 and TCCH$_3$OH = 5.0×10^{15} molecules/cm^2, where both criteria have to be met for the two species to be co-sampled), but sensitivity analysis of these thresholds (**Figure SM5, Table S1**), and the time period in which the plume(s) are sampled, show that our results are robust and relatively insensitive to our choices of these parameters.

In Box 1, the TCCH$_3$OH:TCCO enhancement ratio (M), based on a simple linear least-squares fit, is 0.0036±5.98%, which is similar to the FINN CH$_3$OH:CO fire emissions ratio (0.0031±0.04%). This suggests that the satellite observations of atmospheric enhancements close to the fires are consistent with freshly emitted fire pollution. As the plume propagates eastwards over the Pacific, there is an increase in the TCCH$_3$OH:TCCO enhancement ratio. In Boxes 2, 3 and 4 M is 0.0059±3.13%, 0.0091±1.28% and 0.0081±1.94%, respectively. When using the full range of the IASI TCCH$_3$OH retrievals (i.e. the retrieval values ± the random errors) and recalculating the enhancement ratios, we find that M is perturbed by approximately 10%, which is relatively small, and the regional ratios follow the same tendency. This increase of TCCH$_3$OH with distance, and therefore time, from the fires is suggestive of in-plume chemical production of CH$_3$OH. This is similar to Holzinger et al., (2005) and Coheur et al., (2009), who used aircraft and satellite data respectively, to investigate fire plume CH$_3$OH:CO enhancement ratios suggesting signs of secondary CH$_3$OH production when studying southern European fire plumes. The magnitude of the CH$_3$OH/CO enhancement ratios derived here are consistent with other studies (e.g. Yokelson et al., 1999; Christian et al., 2003; Holzinger et al., 2004; Singh et al., 2004; Karl et al., 2007). Our results imply that IASI detected such secondary formation of CH$_3$OH within the fire plume, but with a robust enhancement across the large portion of the Pacific, on a scale previously not discussed in the literature, to the best of our knowledge. Mixing with background air would likely dilute the plume counteracting some of the downwind increase in CH$_3$OH enhancement relative to CO. This suggests that the in-plume production of CH$_3$OH is likely larger than that suggested by the observed increase in the CH$_3$OH:CO ratio alone. Such large-scale enhancements in CH$_3$OH may have an important influence on the CH$_3$OH budget, impact the oxidative capacity of the remote atmosphere, and potentially the CH$_4$ lifetime (Read et al., 2012). Such secondary methanol production could be driven by the self-reaction of methylperoxy (CH$_3$O$_2$), the reaction of CH$_3$O$_2$ with higher order peroxy (RO$_2$) radicals (Jacob et al., 2005) and OH (Müller et al., 2016), or possibly by less well-established oxidation of organics in the fire plume (Holzinger et al., 2005).

4. Conclusions

The 2019/2020 Australian fires ("black summer") constituted some of the largest regional wildfires in recent decades and produced large quantities of smoke, aerosols and trace gases. Peak fire activity occurred on eucalyptus forest vegetation in south-eastern Australia during December and January. Data from the MetOp-B satellite produced by RAL's NRT processing system show that carbon monoxide (CO) emitted from the fires circumnavigated the entire Southern Hemisphere. Compared with the 2018/2019 fire season, CO levels from the fire-plumes were substantially (and

255   significantly, 99% confidence level) larger by approximately 30-70% over the South Pacific in the
256   November-December-January average.

257   Methanol (CH_3OH), which is difficult to detect in normal circumstances due to its weak absorption
258   signature, was in sufficient abundance to retrieve in-plume column amounts with a good precision.
259   Satellite-observed enhancements in total column CH_3OH relative total column CO show a substantial
260   increase downwind from the fires, over the Pacific Ocean. This is strongly suggestive of CH_3OH
261   production within the plume, on a scale not previously reported, as far as we are aware, with
262   potentially important implications for the methanol budget and oxidative capacity of the remote
263   atmosphere. Elevated levels of CH_4 were also detected in association with the fire-plumes during
264   peak activity in early-mid January 2020, even though the CH_4 emission rate is considerably lower
265   than for CO and perturbations from uniform mixing less than 2%.

266   With future climate and land-use change it is expected that wildfires are going to become more
267   frequent and intense. Therefore, Earth observation (EO), as presented here, is going to be a vital
268   resource to help monitor and understand future wildfire events globally. These EO capabilities will
269   improve with the planned launches of advanced infrared and shortwave spectrometers such as IASI
270   Next Generation and Sentinel 5 on the MetOp Second Generation in polar orbit (ESA, 2020) and the
271   Infrared Sounder and Sentinel 4 on Meteosat Third Generation in geostationary orbit.

284   **References**

285   Akagi, S. K., Yokelson, R. J., Wiedinmyer, C., Alvarado, M. J., Reid, J. S., Karl, T., Crounse, J. D., and
286   Wennberg, P. O. (2011). Emission factors for open and domestic biomass burning for use in
287   atmospheric models. *Atmos. Chem. Phys.* **11**, 4039–72, https://doi.org/10.5194/acp-11-4039-2011.
288

289   Andela, N., Morton, D. C., Giglio, L., Chen, Y., van der Werf, G. R., Kasibhatla, P. S., et al. (2017). A
290   human-driven decline in global burned area. *Science* **356**, 1356-1362. DOI: 10.1126/science.aal4108.
291

292   Australian Bureau of Meteorology. (2020). Annual climate statement 2019.
293   http://www.bom.gov.au/climate/current/annual/aus (last accessed 17/08/2020).
294

295   BBC. 2020. Australia fires: A visual guide to the bushfire crisis. https://www.bbc.co.uk/news/world-
296   australia-50951043 (last accessed 17/08/2020).
297

298 Bowman, M. J. S and Johnston, F. H. 2005. Wildfire Smoke, Fire Management, and Human Health.
299 *EcoHealth* **2**, 76-80. doi: 10.1007/s10393-004-0149-8.

300

301 Bradstock, R. A., Cary, G. J., Davies, I., Lindenmayer, B. D., Price, O. F. and Williams, R. J. 2012.
302 Wildfires, fuel treatment and risk mitigation in Australian eucalypt forests: Insights from landscape-
303 scale simulation. *Journal of Environmental Management* **105**, 66-75.
304 doi.org/10.1016/j.jenvman.2012.03.050.

305

306 Christian, T. J., Kleiss, B., Yokelson, R. J., Holzinger, R., Crutzen, P. J., Hao, W. M., Saharjo, B. H. and
307 Ward, D. E. 2003. Comprehensive laboratory measurements of biomass-burning emissions: 1.
308 Emissions from Indonesian, African, and other fuels. *Journal of Geophysical Research - Atmospheres*
309 **108**, 4719, doi:10.1029/2003JD003704.

310

311 Clarke, H. G., Smith, P. L. and Pitman, A. J. 2010. Regional signatures of future fire weather over
312 eastern Australia from global climate models. International Journal of *Wildland Fire* **20 (4)**, 550-562.
313 doi.org/10.1071/WF10070.

314

315 Clerbaux, C., Boynard, A., Clarisse, L., George, M., Hadji-Lazaro, J., Herbin, H., Hurtmans, D.,
316 Pommier, M., Razavi, A., Turquety, S., Wespes, C. and Coheur, F-P. 2009. Monitoring of atmospheric
317 composition using the thermal infrared IASI/MetOp sounder. *Atmospheric Chemistry and Physics* **9**,
318 6041-6054. doi.org/10.5194/acp-9-6041-2009.

319

320 Coheur, P-F., Clarisse, L., Turquety, S., Hurtmas, D. and Clerbaux, C. 2009. IASI measurements of
321 reactive trace species in biomass burning plumes. *Atmospheric Chemistry and Physics* **9**, 5655-5667.
322 doi.org/10.5194/acp-9-5655-2009.

323

324 Di Virgilio, G., Evans, J. P., Blake, S. A. P., Armstrong, M., Dowdy, A. J., Sharples, J., and McRae,
325 R. 2019. Climate change increases the potential for extreme wildfires. *Geophysical Research*
326 *Letters* **46**, 8517– 8526. doi.org/10.1029/2019GL083699.

327

328 ESA. 2020. Sentinel Overview. https://sentinel.esa.int/web/sentinel/missions (last accessed
329 17/08/2020).

330

331 Giglio, L., Randerson, J. T. and van der Werf, G. R. 2013. Analysis of daily, monthly, and annual
332 burned area using the fourth-generation global fire emissions dataset (GFED4). *Journal of*
333 *Geophysical Research: Biogeosciences* **118**, 317-328. doi:10.1002/jgrg.20042.

334

335 Haikerwal, A., Akram, M., Sim, M. R., Meyer, M., Abramson, M. J. and Dennekamp, M. 2016. Fine
336 particulate matter ($PM_{2.5}$) exposure during a prolonged wildfire period and emergency department
337 visits for asthma. *Respirology* **21**, 88-94. doi:10.1111/resp.12613.

338

339 Holzinger, R., Williams, J., Salisbury, G., Klüpfel, T., de Reus, M., Traub, M., Crutzen, P. J. and
340 Lelieveld, J. 2005. Oxygenated compounds in aged biomass burning plumes over the East
341 Mediterranean: evidence of strong secondary production of methanol and acetone. *Atmospheric*
342 *Chemistry and Physics* **5**, 39-46. doi.org/10.5194/acp-5-39-2005.

343

344 Hope, M. 2020. Australian Burning. *The Lancet Planetary Health* **4 (1)**, E12-E13.

345 dio.org/10.1016/S2542-5196(20)30006-1.

346

347 Illingworth, S. M., Remedios, J.J., Boesch, H., Moore, D. P., Sembhi, H., Dudhia, A. and Walker, J. C.

348 2011. ULIRS, an optimal estimation retrieval scheme for carbon monoxide using IASI spectral

349 radiances: sensitivity analysis, error budget and simulations. *Atmospheric Measurement Techniques*

350 **4**, 269-288. doi:10.5194/amt-4-269-2011.

351

352 Jacob, D. J., Field, B. D., Li, Q., Blake, D. R., de Gouw, J., Warneke, C., Hansel, A., Wisthaler, A., Singh,

353 H. B. and Guenther, A. 2005, Global budget of methanol: Constraints from atmospheric

354 observations, *Journal of Geophysical Research* **110**, D08303, doi:10.1029/2004JD005172.

355

356 Kaiser, J. W., Hell, A., Andreae, M. O., Benedetti, A., Chubarova, N., Jones, L., et al. (2012). Biomass

357 burning emissions estimated with a global fire assimilation system based on observed fire radiative

358 power. *Biogeosciences* **9**, 527-554. https://doi.org/10.5194/bg-9-527-2012.

359

360 Karl, T. G., Christian, T. J., Yokelson, R. J., Artaxo, P., Hao W. M. and Guenther, A. 2007. The Tropical

361 Forest and Fire Emissions Experiment: method evaluation of volatile organic compound emissions

362 measured by PTR- MS, FTIR, and GC from tropical biomass burning. *Atmospheric Chemistry and*

363 *Physics* **7** (22), pp.5883-5897.

364

365 Kiely, L. Spracklen, D. V., Wiedinmyer, C. Conibear, L., Reddington, C. L., Archer-Nicholls, S., Lowe, D.,

366 Arnold, S.A., Knote, C., Khan, M.F., Latif, M. T., Kuwata, M., Budisulistiorini, S. H. and Syaufina, L.

367 2019. New estimate of particulate emissions from Indonesian peat fires in 2015. *Atmospheric*

368 *Chemistry and Physics* **19**, 11105-11121, doi.org/10.5194/acp-19-11105-2019.

369

370 Li, F., Lawrence, D. M. and Bond-Lamberty, B. 2017. Impact of global land surface air temperature

371 and energy budget for the 20th Century due to changes within ecosystems. *Environmental Research*

372 *Letters* **12**, 044014. doi.org/10.1088/1748-9326/aa6685.

373

374 McNorton, J., Chipperfield, M. P., Gloor, M., Wilson, C., Feng, W., Hayman, G. D., Rigby, M.,

375 Krummel, P. B., O'Doherty, S., Prinn, R. G., Weiss, R. F., Young, D., Dlugokencky, E., and Montzka, S.

376 A. (2016). Role of OH variability in the stalling of the global atmospheric CH4 growth rate from 1999

377 to 2006. *Atmos. Chem. Phys.* **16**, 7943–7956, https://doi.org/10.5194/acp16-7943-2016.

378

379 Müller, J-F., Liu, Z., Nguyen, V. S., Stavrakou, T., Harvey, J. N. and Peeters, J. 2016. The reaction of

380 methyl peroxy and hydroxyl radicals as a major source of atmospheric methanol. *Nature*

381 *Communications* **7**, 13213, doi:10.1038/ncomms13213.

382

383 NPI. 2020. National Pollutant Inventory. http://www.npi.gov.au/npidata/action/load/browse-

384 search/criteria/browse-type/Location/year/2019 (last accessed 17/08/2020).

385

386 Ohneiser, K., Ansmann, A., Baars, H., Seifert, P., Barja, B., Jimenez, C., Radenz, M., Teisseire, A.,

387 Floutsi, A., Haarig, M., Foth, A., Chudnovsky, A., Engelmann, R., Zamorano, F., Bühl, J. and

388 Wandering, U. 2020. Smoke of extreme Australian bushfires observed in the stratosphere over Punta

389 Arenas, Chile, in January 2020: optical thickness, lidar ratios, and depolarization ratios at 355 and
390 532 nm. *Atmospheric Chemistry and Physics* **20**, 8003-8015, doi.org/10.5194/acp-20-8003-2020.
391

392 Pitman, A. J., Narisma, G.T. and McAneney, J. 2007. The impact of climate change on the risk of
393 forest and grassland fires in Australia. *Climatic Change* **84**, 383-401. doi:10.1007/s10584-007-9243-6.
394

395 Rabin, S. S., Magi, B. I., Shevliakova, E. and Pacala, S. W. 2015. Quantifying regional, time-varying
396 effects of cropland and pasture on vegetation fire. *Biogeosciences* **12**, 6591-6604.
397 doi.org/10.5194/bg-12-6591-2015.
398

399 RAL Space. 2015. Optimal Estimation Method retrievals with IASI, AMSU and MHS – Final Report
400 Version 5.2. http://cedadocs.ceda.ac.uk/1377/1/iasi_mhs_final_report_v5p2.pdf (last accessed
401 17/08/2020).
402

403 Read, K. A., Carpenter, L. J., Arnold, S. R., Beale, R., Nightingale, P. D., Hopkins, J. R., Lewis, A. C., Lee,
404 J. D., Mendes, L. and Pickering, S. J. 2012. Multiannual observations of acetone, methanol,
405 acetaldehyde in remote tropical Atlantic air: Implications for atmospheric OVOC budgets and
406 oxidative capacity, *Environmental Science Technology* **46**, 20, 11028-11039, doi:10.1021/es302082p.

407 Reisen, F., Meyer, C. P., McCaw, L., Powell, J. C., Tolhurst, K., Keywood, M. D. and Gras, J. L. 2005.
408 Impact of smoke from biomass burning on air quality in rural communities in southern Australia.
409 *Atmospheric Environment* **45 (24)**, 3944-3953. doi.org/10.1016/j.atmosenv.2011.04.060.
410

411 Rowlinson, M, J., Rap, A., Arnold, S. R., Pope, R. J., Chipperfield, M. P., McNorton, J., Forster, P.,
412 Gordon, H., Pringle, K. J., Feng, W., Kerridge, B. J., Latter, B. L. and Siddans, R. 2019. Impact of El
413 Niño–Southern Oscillation on the interannual variability of methane and tropospheric ozone.
414 *Atmospheric Chemistry and Physics* **19**, 8669-8686. doi.org/10.5194/acp-19-8669-2019.
415

416 Siddans, R., Knappett, D., Kerridge, B.J, Waterfall, A., Hurley, J., Latter, B., Boesch, H. and Parker, R.
417 2017. Global height-resolved methane retrievals from the Infrared Atmospheric Sounding
418 Interferometer (IASI) on MetOp, *Atmospheric Measurement Techniques* **10**, 4135-4164, doi**:**
419 10.5194/amt-10-4135-2017.

420 Siddans, R. Knappett, D., Kerridge, B., Latter, B. and Waterfall, A. 2020. STFC RAL methane retrievals
421 from IASI on board MetOp-A, version 2.0. Centre for Environmental Data Analysis, 10 March 2020.
422 doi:10.5285/f717a8ea622f495397f4e76f777349d1.

423

424 Siddaway, J. M. and Petelina, S. V. 2011. Transport and evolution of the 2009 Australian Black
425 Saturday bushfire smoke in the lower stratosphere observed by OSIRIS on Odin. *Journal of
426 Geophysical Research* **116**, D06203. doi:10.1029/2010JD015162.
427

428 Singh, H. B., Salas, L. J., Chatfield, R. B., Czech, E., Fried, A., Walega, J., Evans, M. J., Field, B. D., Jacob,
429 D. J., Blake, D., Heikes, B., Talbot, R., Sachse, G., Crawford, J. H., Avery, M. A., Sandholm, S. and
430 Fuelberg, H. 2004. Analysis of the atmospheric distribution, sources, and sinks of oxygenated volatile
431 organic chemicals based on measurements over the Pacific during TRACE-P. *Journal of Geophysical
432 Research* **109**, D15307, doi:10.1029/2003JD003883.

433

434   SOTE. 2016. Vegetation Land (2016).
435   https://soe.environment.gov.au/theme/land/topic/2016/vegetation-0 (last accessed 17/08/2020).
436
437   UoS. 2020. More than one billion animals killed in Australian bushfires.
438   https://www.sydney.edu.au/news-opinion/news/2020/01/08/australian-bushfires-more-than-one-
439   billion-animals-impacted.html (last accessed 17/08/2020).
440
441   van der Werf, G. R., Randerson, J. T., Giglio, L., Collatz, G. J., Kasibhatla, P. S., Morton, D. C., DeFries,
442   R. S., Jin, Y. and van Leeuwen, T. T. 2010. Global fires emissions and the contributions from
443   deforestation, savannah, forest, agricultural and peat fires (1997-2009). *Atmospheric Chemistry and*
444   *Physics* **10**, 11707-11735. doi:10.5194/acp-10-11707-2010.
445
446   van der Werf, G. R., Randerson, J. T., Giglio, L., van Leeuwen, T. T., Chen, Y., Rogers, B, M., et al.
447   2017. Global fire emission estimates during 1997-2016. *Earth System Science Data* **9**, 697-720.
448   https://doi.org/10.5194/essd-9-697-2017.
449
450   Wiedinmyer, C., Akagi, S. K., Yokelson, R. J., Emmons, L. K., Al-Saadi, A. J., Orlando, J. J. and Soja, A. J.
451   2011. The Fire INventory from NCAR (FINN): a high resolution global model to estimate the
452   emissions from open burning. *Geoscientific Model Development* **4**, 624-641. doi.org/10.5194/gmd-4-
453   625-2011.
454
455   Wooster, M. J., Gaveau, D, L, A., Salim, M. A., Zhang, T., Xu, W., Green, D. C., et al. (2018). New
456   Tropical Peatland Gas and Particulate Emissions Factors Indicate 2015 Indonesian Fires Release Far
457   More Particulate Matter (but Less Methane) than Current Inventories Imply. *Remote Sensing* **10**(4),
458   495. https://doi.org/10.3390/rs10040495.
459
460   Yokelson, R. J., Goode, J. G., Ward, D. E., Susott, R. A., Babbitt, R. E., Wade, D. D., Bertschi, I., Griffith,
461   D. W. T. and Hao, W. M. 1999. Emissions of formaldehyde, acetic acid, methanol, and other trace
462   gases from biomass fires in North Carolina measured by airborne Fourier transform infrared
463   spectroscopy. *Journal of Geophysical Research* **104**, 30109–30125.
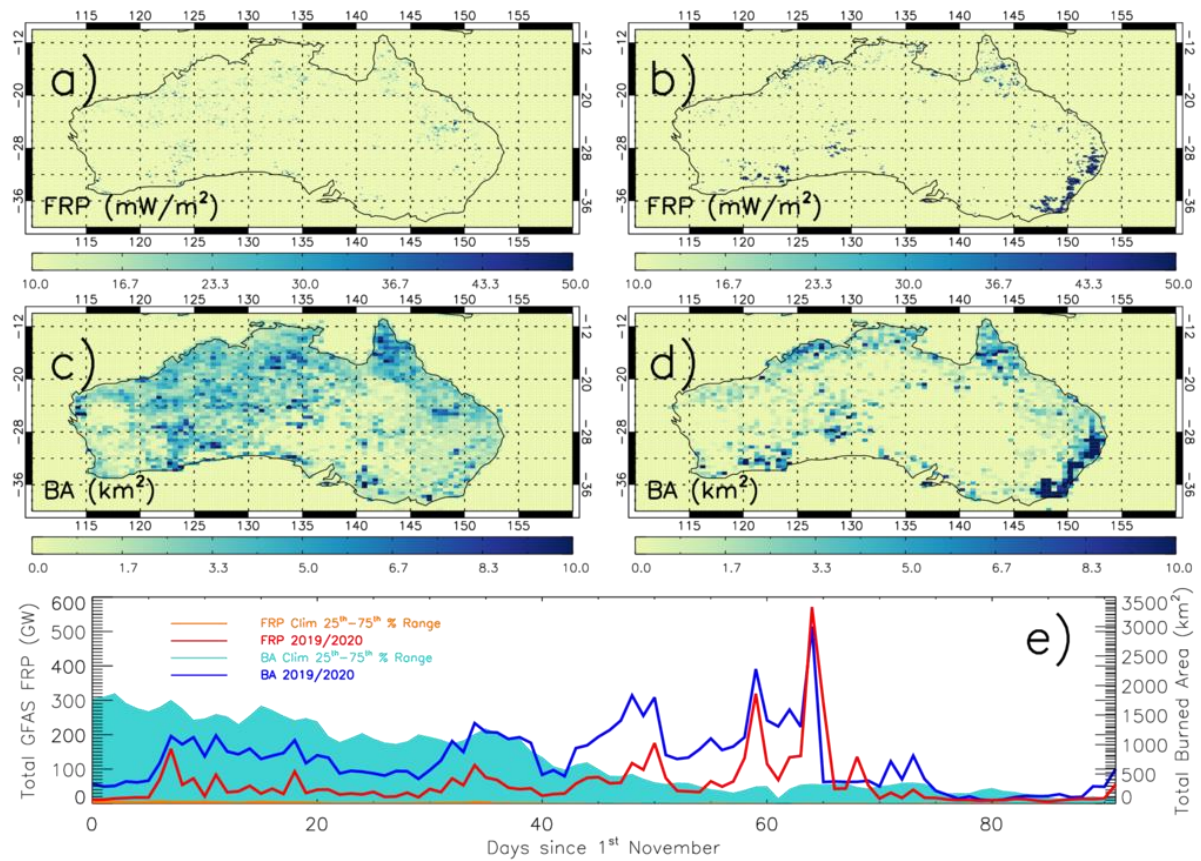464
465

Figures

468   **Figure 1:** Global Fire Assimilation (GFAS) fire radiative power (FRP, mW/m^2) for a) November-
469   December-January (NDJ) climatology (2009-2019) and b) NDJ 2019/2020. Panels c) and d) show Fire
470   INventory from NCAR (FINN) burned area (km^2) for c) NDJ climatology and d) NDJ 2019/2020. Panel
471   e) shows daily time series of accumulated FRP (GW, blue solid line) and BA (km^2, red line) across
472   Australian for NDJ 2019/2020. The orange and light blue shading represent the 25th-75th percentile
473   spread in the climatology for FRP and BA, respectively.
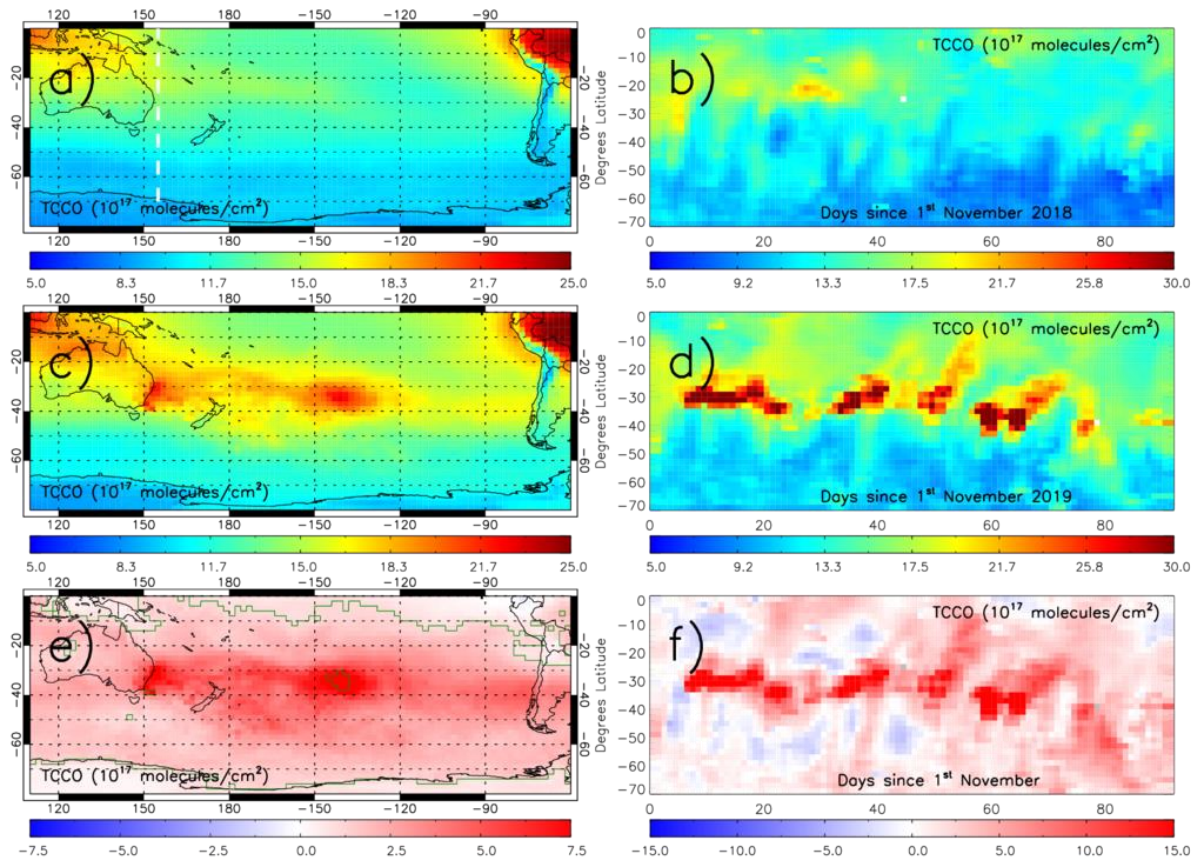
474

475

Figure 2: Infrared Atmospheric Sounding Interferometer (IASI) NDJ total-column carbon monoxide (TCCO, 10^{17} molecules/cm^2) for a) 2018/2019, c) 2019/2020 and e) 2019/2020-2018/2019 difference. Green polygon-outlined regions in panel e) represent statistically significant differences between the fire seasons at the 99% confidence level (CL, based on the Student t-Test) and where absolute differences are greater than 1.0×10^{17} molecules/cm^2. Panels b), d) and f) represent Hovmöller diagrams of IASI TCCO from November – January at 155°E, between 70°S-0°S (white dashed line in panel a)), for 2018/2019, 2019/2020 and 2019/2020-2018/2019 difference, respectively.
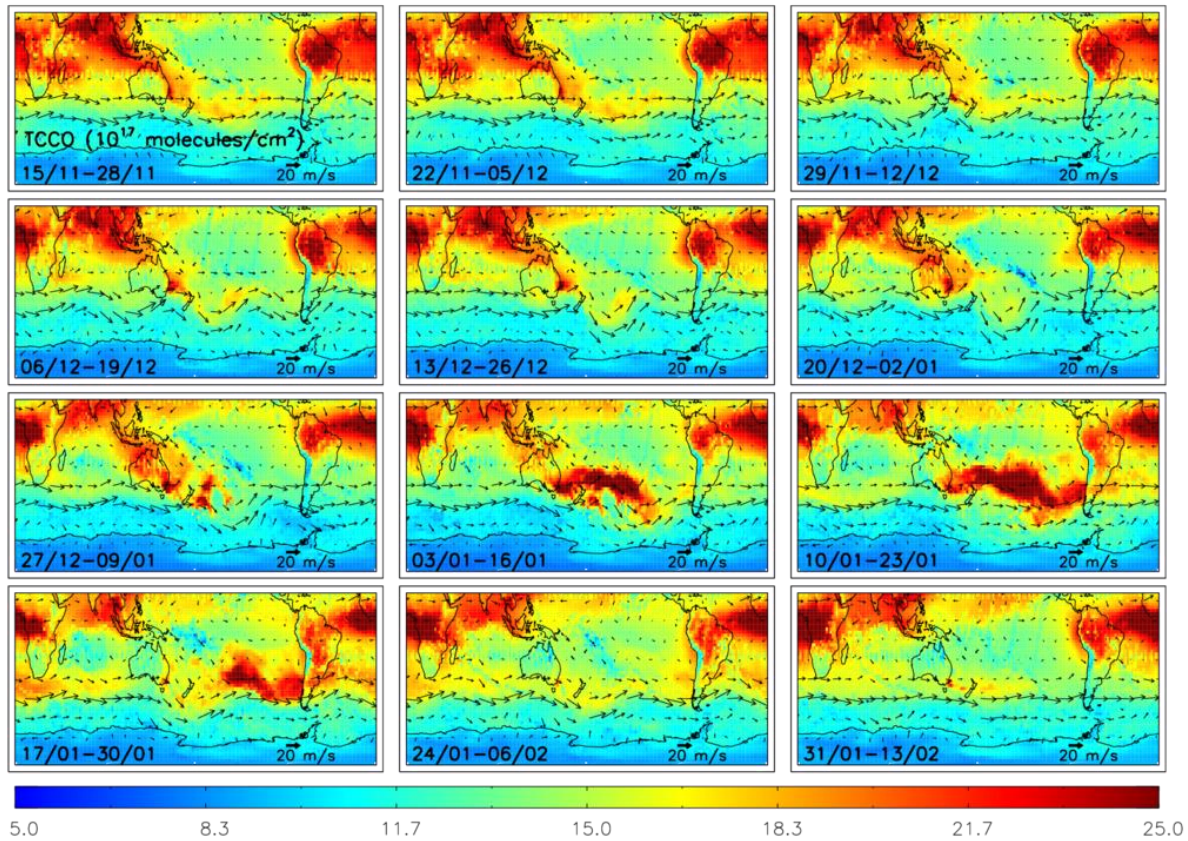
Figure 3: Temporal evolution of the IASI mean TCCO (10^{17}molecules/cm^2) between the 15th November 2019 and 13th February 2020. Each panel represents a 2-week average with a weekly step between the first day of each map. The arrows show 500 hPa winds from the National Centers for Environmental Prediction (NCEP) reanalysis.
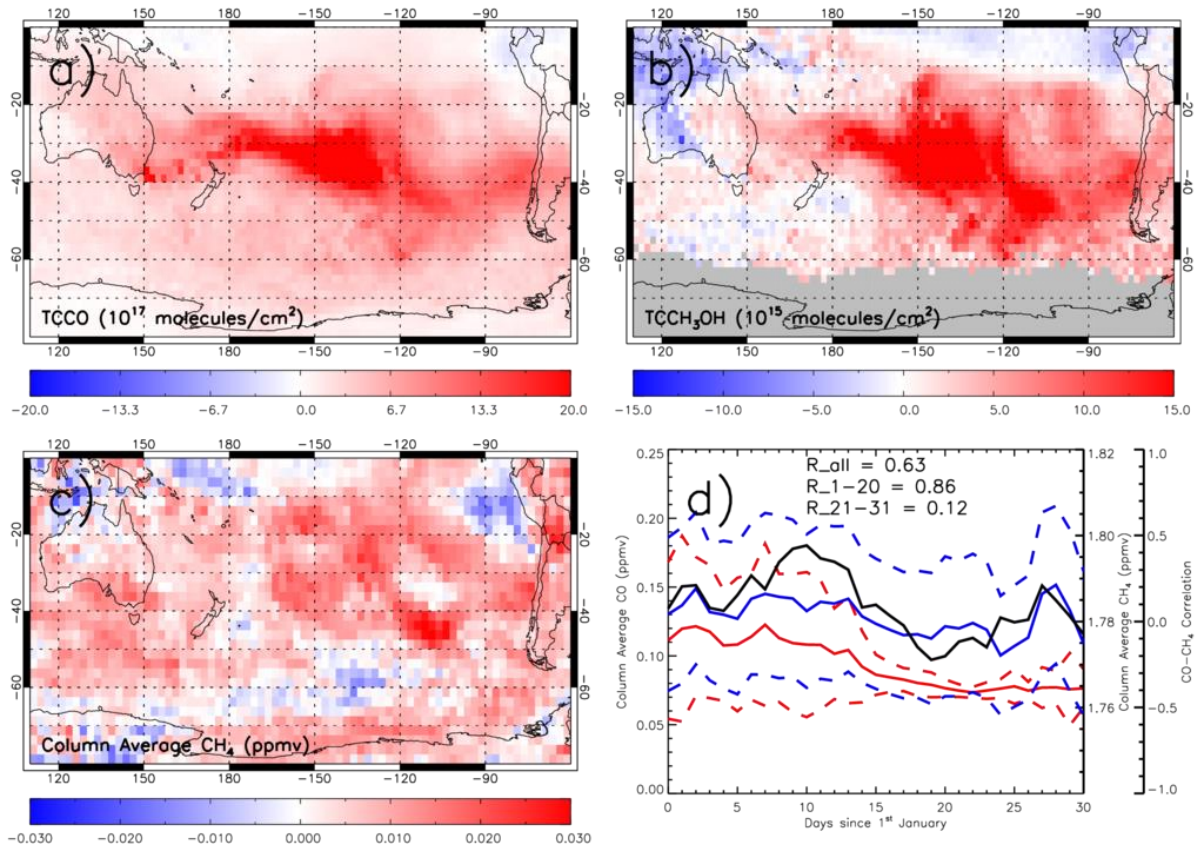
Figure 4: a) IASI two-week (3rd– 16th January) 2020 - 2019 difference a) TCCO (10^{17}molecules/cm^2) and b) total column methanol (TCCH$_3$OH, 10^{15}molecules/cm^2). Grey regions represent missing satellite data (i.e. average values with error terms >15.0×10^{15} molecules/cm^2). c) Two-week (3rd– 16th January 2020) column average methane (CH$_4$, ppmv) anomaly with respect to the de-seasonalised and de-trended multi-annual mean for January (2007-2017). d) Daily time series of spatially averaged in-plume (150°E-90°W, 50-20°S; black box in Figure S4) IASI-observed CO (red) and CH$_4$ (blue) column average mixing ratios for January 2020. In-plume data are defined where CO and CH$_4$ values are both larger than the corresponding thresholds of 0.07 ppmv and 1.75 ppmv. Dashed lines represent the uncertainty range (average ± standard deviation). The black line represents daily spatial correlations between in-plume CO and CH$_4$. R_all, R_1-20 and R_21-31 are the CO-CH$_4$ time series correlations for all of January, 1st-20th January and 21st-31st January, respectively.
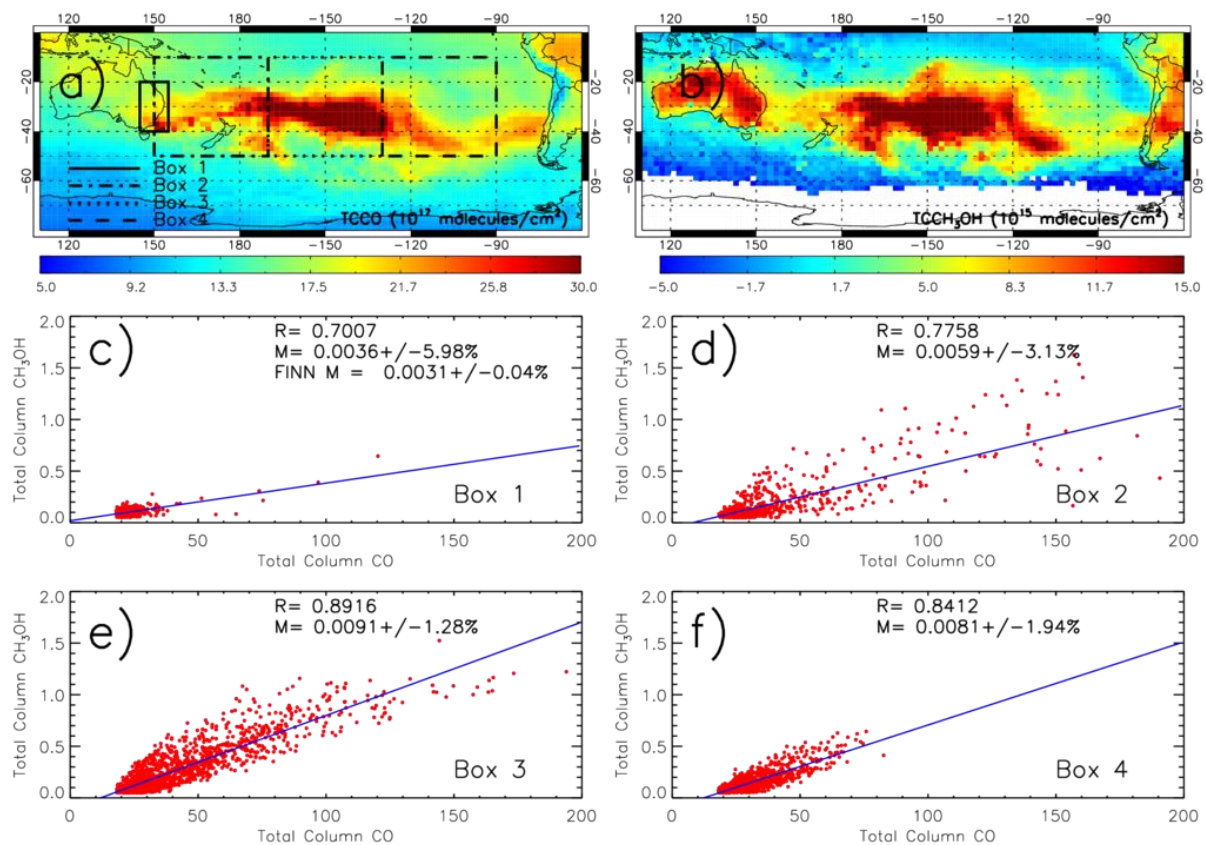
502

Figure 5: a) TCCO and b) TCCH$_3$OH (10^{17} molecules/cm^2) for 1st-17th January 2020. White regions
represent missing satellite data (i.e. average values with error terms >15.0×10^{15} molecules/cm^2).
Panels c) – f) show scatter plots of TCCH$_3$OH versus TCCO within Boxes 1-4 outlined in panel a) with
values of correlation (R) and gradient (enhancement ratio, M) indicated.